pubs.acs.org/Biomac

Article

Scanning Transmission Electron Microscopy in a Scanning Electron Microscope for the High-Throughput Imaging of Biological Assemblies

Kelly A. Parker, Stephanie Ribet, Blaise R. Kimmel, Roberto dos Reis, Milan Mrksich, and Vinayak P. Dravid*

Cite This: https://doi.org/10.1021/acs.biomac.2c00323

Read Online

ACCESS | Metrics & More | Article Recommendations | Supporting Information

ABSTRACT: Electron microscopy of soft and biological materials, or "soft electron microscopy", is essential to the characterization of macromolecules. Soft microscopy is governed by enhancing contrast while maintaining low electron doses, and sample preparation and imaging methodologies are driven by the length scale of features of interest. While cryo-electron microscopy offers the highest resolution, larger structures can be characterized efficiently and with high contrast using low-voltage electron microscopy by performing scanning transmission electron microscopy in a scanning electron microscope (STEM-in-SEM). Here, STEM-in-SEM is demonstrated for a four-lobed protein assembly where the arrangement of the proteins in the construct must be examined. STEM image simulations show the theoretical contrast enhancement at SEM-level voltages for unstained structures, and experimental images with multiple STEM modes exhibit the resolution possible for negative-stained proteins. This technique can be extended to complex protein assemblies, larger structures such as cell sections, and hybrid materials, making STEM-in-SEM a valuable high-throughput imaging method.

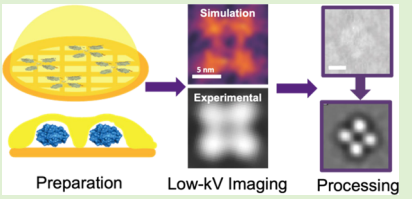

INTRODUCTION

Soft and Biological Imaging. Synthetic biological materials cover a wide range of applications, from bioelectronics for disease detection and therapeutics to biomimetic materials to harness biological properties.[1] When developing new biological materials and assemblies or studying existing structures, researchers aim to assess the relationship between structure, function, and performance. For macromolecules, including proteins and protein assemblies, currently employed characterization techniques aim to understand chemical composition, interaction in solution, folding mechanisms, surface adherence, and the activation of cellular processes, among other properties.[2−4] Contributions to these properties hinge on factors such as size, dispersity, orientation, and morphology. Generally, the molecular weight and dispersity of proteins can be evaluated by techniques such as size exclusion chromatography or dynamic light scattering;[5] however these methods provide information for an ensemble of proteins rather than on a particle-by-particle basis. The relative orientation and morphology of proteins and protein assemblies can be examined by direct imaging techniques. For example, a variety of electron microscopy (EM) methods are utilized to reveal key nanoscale features.

Researchers universally face similar challenges when performing EM on soft and biological structures, or "soft microscopy". These materials have low inherent contrast due to the low atomic number of most components. They are also highly susceptible to electron beam damage due to their low bond energy strength, and to the localized electrons present in the primarily covalent bonds which do not allow for the dissipation of energy from electron excitation without breaking bonds.[6] The typical solution to improve contrast is to increase signal by increasing electron dose, but this furthers the second challenge with beam sensitivity. It is therefore necessary to improve contrast while also maintaining low electron doses to avoid damage. We must further consider how both low-dose imaging methods and contrast enhancement mechanisms impact spatial resolution. One common sample preparation method for the EM of macromolecules is negative staining, where the sample is coated with a heavy metal contrast agent and then dried and imaged at room temperature to both enhance contrast and stabilize structures.[7]

Cryo-EM and Length Scale-Based Characterization. The "gold standard" for biological imaging, cryo-transmission EM (cryo-EM), aids with structure preservation through vitrification.[8] Recent advances in software and hardware for cryo-EM have significantly improved the available contrast and resolution; this includes direct electron detectors, low-dose collection methods, and algorithms for class averaging and single particle reconstruction that allow for both contrast enhancement and three-dimensional structure determination.[9] While uncommon for biological imaging, scanning transmission electron microscopy (STEM) enhances mass-thickness contrast and is compatible with both cryo-EM and room

Received: March 14, 2022
Revised: July 13, 2022

temperature imaging.[10] Despite its prevalence in biological characterization, the resolution of cryo-EM may not be required for sufficient morphological analysis. The length scale of features of interest and the requirements for imaging, including the necessity of screening multiple samples, should be considered when choosing a preparation and imaging method. This work proposes a complementary technique to cryo-EM for the high-throughput imaging of small biological structures and assemblies: imaging at low-voltage using a scanning electron microscope (SEM) with STEM detection (STEM-in-SEM).

Low-Voltage Electron Microscopy: STEM-in-SEM. Low-voltage EM improves image contrast because lower-energy incident electrons have an increased scattering cross-section, meaning that beam electrons have a higher probability of encountering a scattering event before transmitting through the sample.[11] Conventional TEMs generally operate between 80 and 300 kV, except for dedicated low-voltage TEMs; for instrumentation generally available in a microscopy facility, SEM is required to achieve voltages below 30 kV. Both electron sources and electromagnetic lenses are optimized to correct source decoherence for specific voltages, so operating within intended voltage ranges is required. While SEM conventionally uses detectors above the sample for imaging, many SEMs include dedicated STEM detectors below the sample for transmission imaging below 30 kV, and even below 1 kV in certain microscopes. Applicable STEM modes, voltages, and electron dose requirements vary among microscopes, but the appropriate instrumentation is included in numerous commercially available SEMs.

This work focuses on the characterization of a class of biological materials referred to as megamolecules.[12,13] Linear, cyclic, and branched megamolecules are assembled through covalent inhibition reactions between a monomeric protein domain and a targeted covalent inhibitor on a poly(ethylene glycol) (PEG) backbone.[14−16] Here, we use a previously described protein scaffold, known as tetracutinase, as a model system.[17] The linker used to form the tetracutinase megamolecule has four equivalents of a *p*-nitrophenyl phosphonate covalent inhibitor connected by 11 unit PEG arms to a 1,4,7,10-tetraazacyclododecane-1,4,7,10-tetraacetic acid core. Reaction of the nucleophilic serine residue (Ser 120) in the active site of cutinase with the electrophilic phosphonate group yields a covalent linkage, allowing for the atomically precise synthesis of the tetracutinase megamolecule in one-pot. Here we aim not to image the cutinase protein at high resolution, but rather to examine the construct as whole.

This work will examine the efficacy of STEM-in-SEM for the tetracutinase megamolecule, where the individual 3−4 nm protein lobes must be resolvable but sub-nm or sub-Å resolution (as in cryo-EM) is not required. Both image simulations and experimental images demonstrate the application of the method, as well as various considerations to optimize imaging.

MATERIALS AND METHODS

Megamolecule Synthesis. Plasmid construction, protein expression, protein purification, and four-armed linker synthesis for the construction of the tetracutinase megamolecule are previously described.[17] The megamolecule assembly reaction was performed in phosphate buffered saline (PBS) (1× PBS; 2.7 mM KCl, 138 mM NaCl, pH 7.4). To 44 nmol of cutinase protein (44 μM, 1.1 equivalents) was added 10 nmol (10 μM, 1 equivalent) of the four-armed PEG11 linker with terminal *p*-nitrophenyl phosphonate covalent inhibitors. The covalent inhibition reactions between the enzyme and the linker proceeded overnight at room temperature. After the reaction, the crude mixture was purified in a Hi-Load 16/60 Superdex 200 column with a mobile phase of 1× PBS containing 0.02 wt % NaN_3. The pure tetracutinase product fractions were pooled, concentrated using an Amicon Ultra centrifugal filter unit with a 30 kDa cutoff, and diluted to 1 μM in Milli-Q water. Tetracutinase has a molecular weight of 95 kDa.

Sample Preparation. Copper grids for EM were obtained from Electron Microscopy Sciences and have a 5−6 nm amorphous carbon thin film. Tetracutinase was diluted in water to 100 nM and 5 μL of solution was dropcast onto the glow-discharged carbon film for 30 s. The solution was then wicked and washed three times in water. Uranyl formate (UF) was chosen over uranyl acetate and other negative stains because of its comparatively smaller grain size;[7] other stains commonly used for protein contrast enhancement are expected to be compatible with STEM-in-SEM. UF was prepared according to established protocols.[18] Briefly, UF powder was mixed with degassed, deionized water and the pH was slowly increased to approximately 4.5 using NaOH. The stain was continuously covered to avoid precipitation from light. UF was filtered through a 0.2 μM filter and diluted with water to 0.75%. Negative staining was performed by applying 10 μL for 1 s two times and 70 μL for 20 s one time. Grids were wicked between each staining step and partially wicked after the last step, and then left to dry. Grids were stored at room temperature in the dark.

STEM Image Simulation. STEM image simulations were performed by using the PRISM algorithm implemented in MATLAB with interpolation factor 4.[19−21] The probe was set to zero defocus at the entrance surface of the simulation cell. The projected potentials were calculated using a 3D lookup table method[22] using the parameterized atomic potentials given in Kirkland.[23] A slice thickness of 2 Å was used, and an antialiasing aperture was used to zero the pixel intensities at spatial frequencies above 0.5 *qmax during the probe propagation. The cell size is 250 Å × 250 Å × 70 Å and contains 236,034 total atoms. The tetracutinase coordinates were adapted from Zhou et al.,[17] and the amorphous carbon structure was adapted from Ricolleau et al.[24] We modified the original PRISM code to introduce chromatic aberrations (C_c) via relationship with beam spreading d_c in:

$$d_c = C_c \frac{\Delta E}{E_0} \alpha$$

where ΔE is the energy spread of the electron beam, E_0 is the energy of incident electron beam, and α is the convergence semiangle. Bright field (BF) and dark field (DF) images were plotted using collection angles of 0−6 mrad and greater than 80 mrad, respectively. Image intensities were normalized for comparison.

STEM-in-SEM Experimental Imaging. BF images were acquired on the Hitachi SU8030 using a dedicated TEM grid holder for SEM and high-angle annular DF (HAADF) images were acquired on the Thermo Fisher Helios Nanolab Dual Beam SEM/FIB using a six-sample TEM grid stage (Figure 1B). BF images were taken at 20 and 30 kV using a 2 mm STEM aperture and at 10 and 15 kV without an aperture to increase signal. An emission current of 10 μA and 5 mm working distance were used for all images. A liquid nitrogen cold finger on the SU8030 aided in stability and reducing the rate of contamination. HAADF images were acquired from 5 to 15 kV with a working distance of 3 mm without a STEM aperture. Approximately 150 particles were acquired per image with a total scan area of 575 × 400 nm^2. Scan times were 20 s with an additional 30−40 s on average for focus and stigmation, leading to the collection of around 150 particles per minute. Figure S1 details a process flow with approximate timeframes for STEM-in-SEM imaging.

Image Post-Processing. Images were processed using ImageJ and Python. Brightness and contrast were adjusted linearly using the image histogram and noise was reduced using a Gaussian filter. For class averaging, images were first background subtracted and

https://doi.org/10.1021/acs.biomac.2c00323
Biomacromolecules XXXX, XXX, XXX−XXX

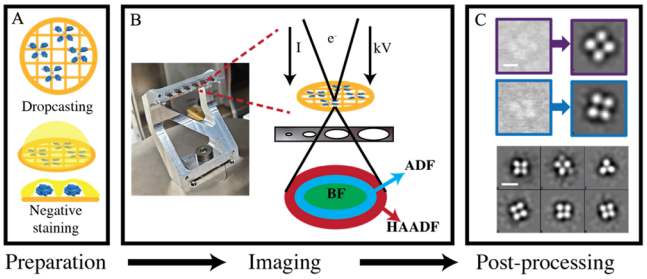

Figure 1. STEM-in-SEM process flow. (A) TEM grid preparation. Tetracutinase was dropcast onto a hydrophilized carbon film TEM grid and stained with 0.75% UF. (B) STEM-in-SEM stage setup. Image shows an example stage for STEM-in-SEM using a six-grid holder, specific to the Thermo Fisher Helios SEM/FIB instrument. Each instrument has a dedicated STEM stage for transmission imaging. Schematic depicts parameters chosen for STEM imaging, including electron voltage, probe current and probe size, apertures, and collection angle for BF, ADF, or HAADF imaging. (C) Postprocessing methods such as class averaging further improve signal-to-noise, shown for 30 kV (top), 20 kV (middle), and 15 kV (bottom panel). Scale bars 5 nm (top) and 10 nm (bottom).

normalized in Python. Class averaging was performed through the EMAN2 package.[25] A neural network was trained using a few references of manually selected megamolecules and background areas. Using the trained algorithm and keeping only high scoring particles, we identified 1818 tetracutinase from 11 images (15 kV) and 1488 tetracutinase from 10 images (30 kV). Using reference free class averaging, each set was sorted and averaged into eight classes.

RESULTS

Application of STEM-in-SEM to Biological Structures. Figure 1 shows the process flow for a STEM-in-SEM setup. Tetracutinase was first dropcast and negative-stained with UF (Figure 1A). Imaging occurred in two separate instruments, both SEMs with STEM detectors but with different detector capabilities; the SU8030 SEM is capable of only BF imaging and the Helios SEM/FIB performs BF, annular DF (ADF), and HAADF imaging. Potential detector collection angles and imaging modes depend on instrument specifications. Voltages from 10 to 30 kV in BF and 5 to 15 kV in HAADF were used to observe differences in contrast and resolution as well as imaging efficacy, and probe size and current could also be modified to tune signal and resolution. Various apertures were used to balance contrast and signal; generally, larger apertures were required at lower voltage because of signal loss. Samples were mounted for STEM-in-SEM using various dedicated TEM grid holders, shown in Figure 1B for the Helios SEM/FIB. This holder allows for the imaging of six samples before opening the chamber for specimen exchange. Finally, post processing was used to identify orientation classes for tetracutinase, similarly to the first stages of single particle analysis.[26] This allows for contrast enhancement across a small number of images, reducing time for data collection and allowing for lower electron doses while imaging. Figure 1C shows various identified classes using STEM-in-SEM images at 30, 20, and 15 kV. Postprocessing involves a variety of methods to improve image quality, from filtering and contrast enhancement to quantitative analysis. STEM images are additionally beneficial because they are dominated by mass−thickness contrast, so in future experiments image intensity can be used to calculate the molecular weight of unstained macromolecules.[27]

Contrast Enhancement with Decreasing Beam Energy. Figure 2A,B show simulated BF and DF STEM images of tetracutinase on an amorphous carbon film from 5 to 30 kV with a 10 mrad convergence semiangle, normalized to compare contrast. Figure S2 shows the same simulations but with a 2 mrad convergence semiangle; most SEM instruments operate somewhere between these two values. Repetition in the background film arises from cycling the structural model of amorphous carbon for the purpose of the simulation; this repetition is not observed in an experimental amorphous film. The improvement in contrast at 5 kV compared to 30 kV is most apparent in BF image simulations. This can be evaluated

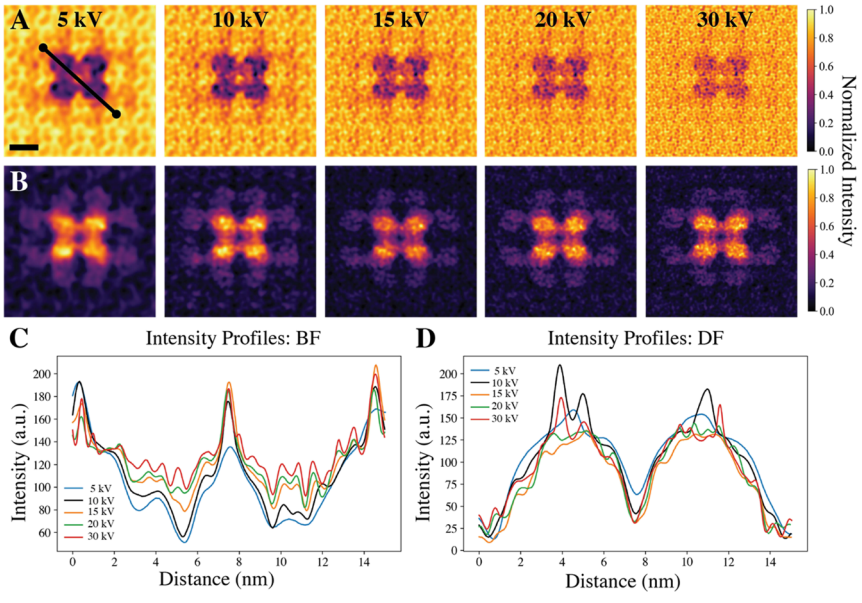

Figure 2. Image simulations with varying voltage. (A) BF (0−6 mrad collection angle) and (B) DF (>80 mrad collection angle) image simulations at 5, 10, 15, 20, and 30 kV using a 10 mrad convergence semiangle. All simulations were normalized to the same scale for comparison. Scale bar 5 nm. Intensity profiles for (C) BF and (D) DF at all voltages provide comparisons across the diagonal of the structure, as shown in panel A.

https://doi.org/10.1021/acs.biomac.2c00323
Biomacromolecules XXXX, XXX, XXX−XXX

using the intensity profiles in Figure 2C, where the normalized intensities of the carbon film at the far ends of the profile are similar across all simulations and the troughs representing the lobes of the proteins are deepest for 5 kV and most shallow for 30 kV. Interestingly, this difference in contrast is less visually apparent for DF simulations; the intensity profiles in Figure 2D reveal the highest contrast for 10 kV followed by 30 and 5 kV. HAADF imaging is particularly sensitive to atomic number, so these simulations may indicate diminishing returns when the structure of interest is similar in atomic number to the support film.

Image simulations also highlight the decrease in resolution at lower voltage. These simulations do not introduce lens aberrations or other practical limitations on resolution; therefore, this reduction in resolution occurs only because of the voltage effects in the calculation of the contrast transfer function, which defines the shape of the STEM probe.[28] The intensity profiles for both BF and DF simulations in Figure 2C,D can also be used to evaluate resolution as details in the amorphous carbon film and the lobes of the protein are smoothed out with decreasing voltage.

Practical Application of STEM-in-SEM. Experimental STEM-in-SEM images of tetracutinase stained with UF are shown in Figure 3. Images of additional proteins and protein

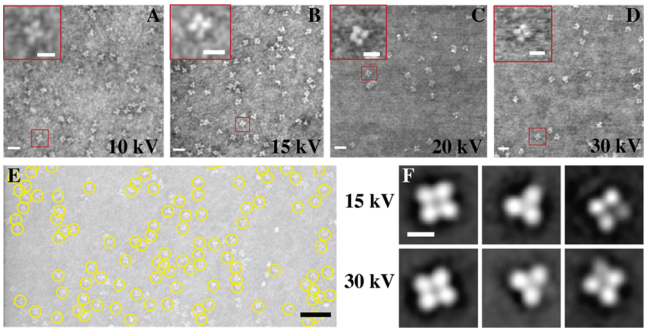

Figure 3. Experimental images and class averages. (A–D) BF STEM images of tetracutinase acquired on the SU8030 SEM at 10, 15, 20, and 30 kV. Scale bars 20 and 10 nm (inset). (E) BF STEM image at 30 kV showing particles picked for class averaging. Scale bar 50 nm. (F) Selected classes after class averaging at 15 and 30 kV. Classes included four-lobed structures, apparent three-lobed structures that may either depict a hidden lobe in the background or indicate a decreased yield of four-lobed structures in synthesis, and structures where a fourth lobe is visible but on a different *z*-plane than the other three lobes. Scale bar 5 nm.

assemblies with higher and lower molecular weights than that of tetracutinase are provided in Figure S3. The BF STEM images in Figure 3A–D demonstrate the capabilities of the SU8030 SEM at 10, 15, 20, and 30 kV; imaging under 10 kV was not possible with the current setup because of low signal and a high rate of carbon contamination. Low signal can be mitigated by using a thinner support film, as much of the transmission thickness arises from the carbon film in this case. The images demonstrate reduced resolution and image clarity at 10 kV compared to 30 kV, but also show that the four cutinase lobes are resolvable at all voltages.

We additionally observed more changes in background contrast at low voltage from variations in both the thickness of the carbon film and thickness of the stain; this is expected because the increased scattering cross-section leads to a higher dependence on the mass and thickness of the structure. Lower voltages also suffered from more organic contamination while imaging, as the rate of contamination is expected to increase with lower electron energy due to more inelastic scattering.[29] This leads to practical challenges in achieving optimal focus and stigmation while imaging and may result in an apparent reduction in resolution. Direct comparison to simulated images in terms of ultimate contrast and resolution is not possible because experiments were performed on UF-stained samples, necessary to preserve protein structures. We did not observe significant differences in contrast with voltage during experimental imaging; this was expected because the uranyl contrast agent contributes greatly to contrast enhancement, overwhelming additional contrast from decreased voltage. Low-voltage contrast enhancement would likely be more pronounced with samples that do not require staining or fixation, or when using a cryo-SEM setup.

In addition to the contrast gained by decreasing voltage, signal-to-noise can be improved using class averaging. As shown in Figure 3E, particles from BF images at two voltages were chosen automatically and checked manually across a series of images under identical imaging conditions. These could be assembled into classes and averaged for enhanced contrast, as shown for three representative classes at 15 and 30 kV in Figure 3F. All identified classes are shown in Figure S4. BF images were chosen for class averaging because higher signal improved the quality of images when compared with DF imaging. Class averaging with HAADF ("z-contrast") STEM images would be beneficial for structures where an atomic number difference exists, as it could improve the signal-to-noise ratio between the two components.

Impact on Spatial Resolution. The work thus far has primarily focused on changes in contrast with electron beam voltage. Spatial resolution must also be considered when evaluating the practicality of STEM-in-SEM for nanoscale biological structures. Figure 4A–C show HAADF STEM images of UF-stained tetracutinase acquired on the Helios

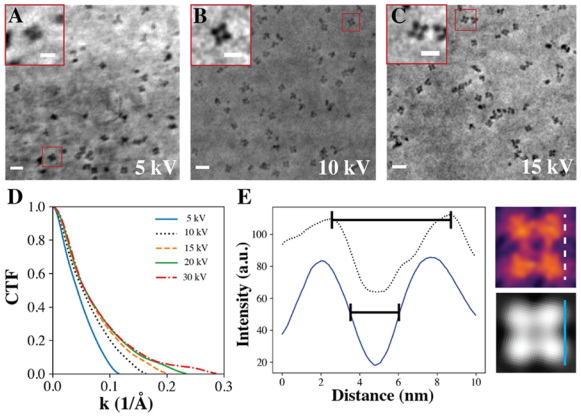

Figure 4. Impact of voltage on spatial resolution. (A–C) HAADF STEM images at 5, 10, and 15 kV acquired using the Helios SEM/FIB. Decreased resolution is apparent at 5 kV, potentially due to either chromatic aberration in the condenser lenses or difficulty in adjusting focus and stigmation as a result of low signal. Scale bars 20 and 10 nm (inset). (D) STEM contrast transfer function calculated from 5 to 30 kV demonstrating the increase in expected resolution with increasing beam voltage. (E) Intensity profiles for simulated image (top, dashed black line) of unstained structure and experimental class-averaged image (bottom, solid blue line) of the UF-stained structure.

https://doi.org/10.1021/acs.biomac.2c00323
Biomacromolecules XXXX, XXX, XXX–XXX

SEM/FIB at 5, 10, and 15 kV. The instrument requires longer working distances than used here at 20 kV and above, so the resolution at higher voltage was not comparable. As with BF imaging, we observe a resolution decrease with lower voltage, but the four lobes are still resolvable. This reduction in resolution may be due to an increase in the impact of chromatic aberration at lower voltage, or it could arise primarily from practical limitations resulting from low signal and a high rate of organic contamination.

Chromatic aberration occurs when electrons are deflected differently by electromagnetic lenses based on variations in electron energy. While chromatic lens aberrations from energy spread increase in impact over spherical aberrations at low-voltage, chromatic aberration is not expected to significantly decrease resolution at 5 kV and higher at this length scale; chromatic aberration may become more important at voltages nearing 1 kV or when imaging smaller length scales.[30] This is confirmed by simulations in Figure S5, which show no discernable difference when a realistic amount of chromatic aberration is added at 5 kV. These simulations were performed on unstained structures and do not account for the impact of the UF stain on spatial resolution. One benefit of STEM over TEM is the replacement of the image-forming postspecimen lenses with STEM detectors, reducing aberrations from energy spread after electrons transmit through the sample.

As shown in Figure 4D, the STEM contrast transfer function limits spatial resolution according to voltage; this function calculates the phase shift in the electron wave resulting from lens aberrations.[20] The maximum value for k (1/Å), the spatial frequency, represents the highest possible resolution in real space. This indicates that the lower the voltage, the lower the maximum spatial frequency, translating to decreased spatial resolution. However, a maximum spatial frequency of approximately 0.1 $Å^{-1}$ at 5 kV translates to a 10 Å (1 nm) information limit, sufficient resolution to image an assembly of 3−4 nm proteins. Electron source decoherence varies from voltage-to-voltage and is microscope dependent, so the shape of the beam and the effectiveness of the lenses in correcting beam shape can result in limitations on spatial resolution at certain voltages.

Fixation and staining are essential for imaging at room temperature, and negative staining reduces resolution according to the grain size of the stain; for UF, this error is around 0.5 to 1 nm.[7] To evaluate the effect of staining on resolution, Figure 4E compares intensity profiles along the side of two protein lobes for a class-averaged image and simulated image at 15 kV. The simulated image was Gaussian filtered to remove details in the protein and background film for comparison. The distance between the brightest points on each protein lobe was similar, at around 6 to 6.5 nm for the experimental and simulated images. The full width at half minimum was used as an approximation for the distance separating the lobes and measured to be around 2 nm for the class-averaged image and 3 nm for the simulated, unstained image. This 1 nm difference aligns with the 0.5−1 nm error from negative staining. Despite the impact of staining on resolution, it is an effective method when imaging assemblies as opposed to focusing on fine features of individual proteins.

DISCUSSION

Further Considerations for STEM-in-SEM of Biological Structures. There are several factors outside of contrast and spatial resolution to consider in the STEM-in-SEM approach. First, beam-mediated damage occurs primarily by two mechanisms − knock-on damage and radiolytic damage. Knock-on damage from elastic scattering is solely dependent on electron energy, so low-kV operation is a principal method for damage reduction in knock-on-sensitive compounds.[31] The primary damage mechanism in organic samples, however, is ionization damage from inelastic scattering. The interaction of incident electrons with the sample leads to electron transitions to excited states, and valence band holes are filled quickly in conducting materials. In organic materials, the secondary and Auger electrons produced by inelastic interactions carry sufficient energy to break atomic bonds, leading to radiolytic decomposition.[32] Decreasing the incident electron voltage, and therefore energy, decreases knock-on damage but increases radiolytic damage.[33] Electron doses in this study are believed to be on the order of 1×10^6 electrons/$Å^2$ or higher; depending on the ability to control probe current according to the instrument specifications, this may be prohibitive for unstained, beam sensitive structures.

Additional challenges exist when performing STEM-in-SEM on biological structures. As indicated previously, organic contamination occurs more rapidly at lower voltage because of increased inelastic scattering.[31] Contamination introduces practical challenges during focusing and stigmation at high magnification, ultimately reducing resolution. The effect of contamination can be quantified through changes in resolution, structural features, and contrast between subsequent scans. While multiple scans of a single field of view were not needed because of the high degree of homogeneity and consistent dispersion of tetracutinase, contamination is a limiting factor for samples where numerous scans of the same area are necessary. Figure S6 displays the effect of contamination on subsequent scans of the same area. Finally, signal decreases with voltage because fewer electrons maintain the energy to transmit fully through the sample. A low signal similarly inhibits proper focus and stigmation for optimal resolution and also limits the ability to image thick specimens.

Contrast enhancement with staining can impact structure and image quality depending on the requirements for imaging; most negative stains are applied at low pH and require drying, and this can lead to structure breakup and shrinkage.[34] As demonstrated, negative stains additionally reduce image resolution because of the grain size of the stain.[7] It is possible to image unstained, dried structures, but drying can lead to unfolding in the case of proteins or structural collapse in the case of cells and tissue without fixation from the stain.[35] While this work demonstrates experimental imaging only on stained structures, where the improvement in contrast derives mostly from the stain and less from the decrease in voltage, unstained imaging can be highly effective in various soft materials including polymers or in hybrid materials where contrast can be improved for the soft component compared with the hard component. Unstained STEM-in-SEM may also be applied to structures embedded in a support material or using environmental SEM, where the contrast enhancement is derived largely from the decrease in beam voltage.

Attributes of STEM-in-SEM. Any imaging technique for biological structures will undoubtedly be compared to cryo-EM, which offers the highest resolution possible for protein structural characterization when combined with direct electron detectors. STEM-in-SEM is proposed for a different use case than that of cryo-EM and is particularly beneficial for soft and biological structures at larger length scales than that of single

https://doi.org/10.1021/acs.biomac.2c00323
Biomacromolecules XXXX, XXX, XXX−XXX

proteins and for the screening of many samples. STEM imaging offers advantages over TEM—contrast in STEM only depends on the mass and thickness of the sample, often making images more interpretable without phase or diffraction contrast. STEM is also highly multimodal. Where TEM only allows for the capture of one image at a time, STEM can simultaneously acquire multiple modes of detection, chemical signals through spectroscopy, diffraction information, and more. STEM is also compatible with sparse scanning, where a subset of pixels is intelligently collected by dynamic sampling to reduce the total electron dose and scanning time.[36]

STEM-in-SEM has additional advantages beyond dedicated STEM. Several signals collected in SEM, including backscattered and secondary electrons, are uncommon in STEM or TEM instruments. Though not demonstrated here, these signals provide valuable compositional contrast through atomic number-dependent backscattered imaging and topographical information through surface-sensitive secondary electron imaging. The large SEM chamber also offers versatility in the size and shape of samples. STEM-in-SEM is high-throughput because of the nature of SEM specimen exchange and the availability of multigrid holders, and SEMs are generally lower in cost when compared with dedicated STEM, TEM, and cryo-EM instruments. For structures where the length scale does not require the level of resolution attainable with cryo-EM, STEM-in-SEM is a valuable complementary high-throughput technique.

CONCLUSIONS

Examining the relevant length scale of materials and the resolution required by imaging allows for the use of sample preparation and imaging methodologies that are generally underutilized in biological imaging. This work offers an analysis of the STEM-in-SEM method for macromolecular assemblies, specifically the tetracutinase megamolecule. The technique focuses on the high-throughput imaging of negative-stained structures where the spatial resolution afforded by cryo-EM is not required for successful morphological analysis. In the case of tetracutinase, imaging was used to identify individual cutinase lobes and their orientation in the structure. We therefore suggest STEM-in-SEM not as a competitor to cryo-EM, but as a complementary technique for the contrast enhancement and high-throughput imaging of similar macromolecular assemblies. The ability to quickly change samples, especially in the case of the six-grid Helios SEM/FIB sample holder, allows for fast screening of numerous grids; depending on the required image resolution, promising samples can then be selected for cryo-EM or various other techniques. The equipment for STEM-in-SEM is also available in commercial SEMs at a drastically lower cost than that of dedicated cryo-instruments and the necessary direct electron detectors, offering an approach for macromolecular imaging that is more attainable for individual research labs. While cryo-EM might be necessitated by other factors, such as fragility during sample preparation or the requirement of precise sample size measurements, STEM-in-SEM is an ideal method for the contrast enhancement and high-throughput imaging of megamolecules, other protein assemblies, and soft materials in general from the nanometer to micron length scale.

Other methodologies to enhance contrast and further reduce dose can be implemented in conjunction with SEM; this includes phase retrieval imaging with the introduction of a diffraction detector, where the image can be reconstructed using far-field electron diffraction patterns collected with each probe position.[37] We can also leverage the abundance of signals available in SEM, including backscattered imaging, spectroscopic methods such as energy dispersive X-ray spectroscopy, and environmental SEM. While these techniques may not afford the resolution necessary to image protein assemblies, depending on the instrument and detector spatial resolution, they can be highly useful for imaging at larger length scales. The possibility for high-throughput, high-contrast STEM imaging was demonstrated on a protein assembly as a model system to exemplify the high resolution possible; in conjunction with the wealth of techniques and signals available in SEM, often collected simultaneously, the STEM-in-SEM method is highly promising for a range of soft and biological structures.

ASSOCIATED CONTENT

Supporting Information

The Supporting Information is available free of charge at https://pubs.acs.org/doi/10.1021/acs.biomac.2c00323.

Imaging process flow, additional simulated images, full class average sets, experimental images of various structures, and images showing the effect of organic contamination (PDF)

AUTHOR INFORMATION

Corresponding Author

Vinayak P. Dravid − *Department of Materials Science and Engineering, Northwestern University, Evanston, Illinois 60208, United States; Northwestern University Atomic and Nanoscale Characterization Experimental (NUANCE) Center, Northwestern University, Evanston, Illinois 60208, United States;* orcid.org/0000-0002-6007-3063; Email: v-dravid@northwestern.edu

Authors

Kelly A. Parker − *Department of Materials Science and Engineering, Northwestern University, Evanston, Illinois 60208, United States;* orcid.org/0000-0003-0962-7582

Stephanie Ribet − *Department of Materials Science and Engineering, Northwestern University, Evanston, Illinois 60208, United States;* orcid.org/0000-0002-7117-066X

Blaise R. Kimmel − *Department of Chemical and Biological Engineering, Northwestern University, Evanston, Illinois 60208, United States;* orcid.org/0000-0002-9582-9887

Roberto dos Reis − *Department of Materials Science and Engineering, Northwestern University, Evanston, Illinois 60208, United States; Northwestern University Atomic and Nanoscale Characterization Experimental (NUANCE) Center, Northwestern University, Evanston, Illinois 60208, United States*

Milan Mrksich − *Department of Biomedical Engineering and Department of Chemistry, Northwestern University, Evanston, Illinois 60208, United States;* orcid.org/0000-0002-4964-796X

Complete contact information is available at: https://pubs.acs.org/10.1021/acs.biomac.2c00323

Notes

The authors declare no competing financial interest.

https://doi.org/10.1021/acs.biomac.2c00323
Biomacromolecules XXXX, XXX, XXX−XXX

■ ACKNOWLEDGMENTS

K.A.P. and B.R.K. acknowledge the National Science Foundation Graduate Research Fellowship under Grant DGE-1842165, the ARO MURI W911NF-18-1-0200, and the Ryan Fellowship. K.A.P. acknowledges the Air Force Center of Excellence for Advanced Bioprogrammable Nanomaterials Grant AFRL FA8650-15-2-5518. S.M.R. acknowledges funding from 3M and the Ryan Fellowship. Research reported in this publication was supported by the National Cancer Institute of the National Institutes of Health under Award Number U54CA199091. The content is solely the responsibility of the authors and does not necessarily represent the official views of the National Institutes of Health. This work used facilities of the Integrated Molecular Structure Education and Research Center, which received financial support from the State of Illinois. This work made use of the BioCryo and Keck-II facilities of Northwestern University's NU*ANCE* Center, which has received support from the Soft and Hybrid Nanotechnology Experimental (SHyNE) Resource (NSF ECCS-1542205); the MRSEC program (NSF DMR-1720139) at the Materials Research Center; the International Institute for Nanotechnology (IIN); and the State of Illinois, through the IIN. This research was supported in part through the computational resources and staff contributions provided for the Quest high performance computing facility at Northwestern University which is jointly supported by the Office of the Provost, the Office for Research, and Northwestern University Information Technology. The authors would like to thank Dr. Benjamin Myers, Dr. Paul Smeets and Tirzah Abbott for their help and advice during image collection and Zhaoyi Gu, Yasmine Zubi, and Prof. Jared Lewis for the use of proteins for imaging.

■ REFERENCES

(1) Le Feuvre, R. A.; Scrutton, N. S. A living foundry for Synthetic Biological Materials: A synthetic biology roadmap to new advanced materials. *Synth. Syst. Biotechnol.* **2018**, *3*, 105−112.
(2) Sánchez-Vioque, R.; Clemente, A.; Vioque, J.; Bautista, J.; Millán, F. Protein isolates from chickpea (*Cicer arietinum* L.): chemical composition, functional properties and protein characterization. *Food Chem.* **1999**, *64*, 237−243.
(3) Hawe, A.; Sutter, M.; Jiskoot, W. Extrinsic Fluorescent Dyes as Tools for Protein Characterization. *Pharm. Res.* **2008**, *25*, 1487−1499.
(4) Gronthos, S.; Franklin, D. M.; Leddy, H. A.; Robey, P. G.; Storms, R. W.; Gimble, J. M. Surface protein characterization of human adipose tissue-derived stromal cells. *J. Cell. Physiol.* **2001**, *189*, 54−63.
(5) Ahrer, K.; Buchacher, A.; Iberer, G.; Josic, D.; Jungbauer, A. Analysis of aggregates of human immunoglobulin G using size-exclusion chromatography, static and dynamic light scattering. *J. Chromatogr. A* **2003**, *1009*, 89−96.
(6) Isaacson, M.; Johnson, D.; Crewe, A. V. Electron beam excitation and damage of biological molecules: Its implications for specimen damage in electron microscopy. *Radiat. Res.* **1973**, *55*, 205−224.
(7) Ohi, M.; Li, Y.; Cheng, Y.; Walz, T. Negative staining and image classification — powerful tools in modern electron microscopy. *Biol. Proced. Online* **2004**, *6*, 23−34.
(8) Wolf, S. G.; Houben, L.; Elbaum, M. Cryo-scanning transmission electron tomography of vitrified cells. *Nat. Methods* **2014**, *11*, 423−428.
(9) Nogales, E. The development of cryo-EM into a mainstream structural biology technique. *Nat. Methods* **2016**, *13*, 24−27.
(10) Thomas, D.; Schultz, P.; Steven, A. C.; Wall, J. S. Mass analysis of biological macromolecular complexes by STEM. *Biol. Cell* **1994**, *80*, 181−192.
(11) Hall, C. E. In *Introduction to Electron Microscopy*; McGraw-Hill Publishing Co.: New York, NY & London, 1953.
(12) Modica, J. A.; Skarpathiotis, S.; Mrksich, M. Modular Assembly of Protein Building Blocks to Create Precisely-Defined Megamolecules. *ChemBioChem* **2012**, *13*, 2331.
(13) Kimmel, B. R.; Mrksich, M. Development of an Enzyme-Inhibitor Reaction Using Cellular Retinoic Acid Binding Protein II for One-Pot Megamolecule Assembly. *Chem. − Eur. J.* **2021**, *27*, 17843−17848.
(14) Modica, J. A.; Lin, Y.; Mrksich, M. Synthesis of Cyclic Megamolecules. *J. Am. Chem. Soc.* **2018**, *140*, 6391−6399.
(15) Kimmel, B. R.; Modica, J. A.; Parker, K.; Dravid, V.; Mrksich, M. Solid-Phase Synthesis of Megamolecules. *J. Am. Chem. Soc.* **2020**, *142*, 4534−4538.
(16) Metcalf, K. J.; Kimmel, B. R.; Sykora, D. J.; Modica, J. A.; Parker, K. A.; Berens, E.; Dai, R.; Dravid, V. P.; Werb, Z.; Mrksich, M. Synthetic Tuning of Domain Stoichiometry in Nanobody-Enzyme Megamolecules. *Bioconjugate Chem.* **2021**, *32*, 143−152.
(17) Zhou, S.; He, P.; Dhindwal, S.; Grum-Tokars, V. L.; Li, Y.; Parker, K.; Modica, J. A.; Bleher, R.; Dos Reis, R.; Zuchniarz, J.; Dravid, V. P.; Voth, G. A.; Roux, B.; Mrksich, M. Synthesis, Characterization, and Simulation of Four-Armed Megamolecules. *Biomacromolecules* **2021**, *22*, 2363−2372.
(18) Booth, D. S.; Avila-Sakar, A.; Cheng, Y. Visualizing Proteins and Macromolecular Complexes by Negative Stain EM: from Grid Preparation to Image Acquisition. *J. Visualized Exp.* **2011**, *58*, 3227.
(19) Ophus, C. A fast image simulation algorithm for scanning transmission electron microscopy. *Adv. Struct. Chem. Imaging* **2017**, *3*, 13.
(20) Pryor, A., Jr.; Ophus, C.; Miao, J. A streaming multi-GPU implementation of image simulation algorithms for scanning transmission electron microscopy. *Adv. Struct. Chem. Imaging* **2017**, *3*, 15.
(21) Pelz, P.; Rakowski, A.; DaCosta, L. R.; Savitzky, B.; Scott, M.; Ophus, C. A Fast Algorithm for Scanning Transmission Electron Microscopy Imaging and 4D-STEM Diffraction Simulations. *Microsc. Microanal.* **2021**, *27*, 835−848.
(22) DaCosta, L. R.; Brown, H. G.; Pelz, P. M.; Rakowski, A.; Barber, N.; O'Donovan, P.; McBean, P.; Jones, L.; Ciston, J.; Scott, M. C.; Ophus, C. Prismatic 2.0−Simulation software for scanning and high resolution transmission electron microscopy (STEM and HRTEM). *Micron* **2021**, *151*, No. 103141.
(23) Kirkland, E. J. *Advanced Computing in Electron Microscopy*, 3rd ed.; Springer Science & Business Media: New York, NY, 2020.
(24) Ricolleau, C.; Le Bouar, Y.; Amara, H.; Landon-Cardinal, O.; Alloyeau, D. Random vs realistic amorphous carbon models for high resolution microscopy and electron diffraction. *J. Appl. Phys.* **2013**, *114*, 213504.
(25) Tang, G.; Peng, L.; Baldwin, P. R.; Mann, D. S.; Jiang, W.; Rees, I.; Ludtke, S. J. EMAN2: an extensible image processing suite for electron microscopy. *J. Struct. Biol.* **2007**, *157*, 38−46.
(26) Cong, Y.; Ludtke, S. J. Single Particle Analysis at High Resolution. *Methods Enzymol.* **2010**, *482*, 211−235.
(27) Sousa, A. A.; Leapman, R. D. Quantitative STEM mass measurement of biological macromolecules in a 300 kV TEM. *J. Microsc.* **2007**, *228*, 25−33.
(28) Lentzen, M. Contrast Transfer and Resolution Limits for Sub-Angstrom High-Resolution Transmission Electron Microscopy. *Microsc. Microanal.* **2008**, *14*, 16−26.
(29) Kumao, A.; Hashimoto, H.; Shiraishi, K. Studies on Specimen Contamination by Transmission Electron Microscopy. *J. Electron Microsc.* **1981**, *30*, 161−170.
(30) Rose, H.; Wan, W. Aberration Correction in Electron Microscopy. In *Proceedings of the 2005 Particle Accelerator Conference*, 2005; pp 44−48, DOI: 10.1109/PAC.2005.1590354.
(31) Kaiser, U.; Biskupek, J.; Meyer, J. C.; Leschner, J.; Lechner, L.; Rose, H.; Stöger-Pollach, M.; Khlobystov, A. N.; Hartel, P.; Müller, H.; Haider, M.; Eyhusen, S.; Benner, G. Transmission electron microscopy at 20 kV for imaging and spectroscopy. *Ultramicroscopy* **2011**, *111*, 1239−1246.

https://doi.org/10.1021/acs.biomac.2c00323
Biomacromolecules XXXX, XXX, XXX−XXX

(32) Egerton, R. F. Control of radiation damage in the TEM. *Ultramicroscopy* **2013**, *127*, 100−108.
(33) Majorovits, E.; Angert, I.; Kaiser, U.; Schröder, R. R. Benefits and Limitations of Low-kV Macromolecular Imaging of Frozen-Hydrated Biological Samples. *Biophys. J.* **2016**, *110*, 776−784.
(34) Kiselev, N. A.; Sherman, M. B.; Tsuprun, V. L. Negative staining of proteins. *Electron Microsc. Rev.* **1990**, *3*, 43−72.
(35) Denavi, G.; Tapia-Blácido, D. R.; Añón, M. C.; Sobral, P. J. A.; Mauri, A. N.; Menegalli, F. C. Effects of drying conditions on some physical properties of soy protein films. *J. Food Eng.* **2009**, *90*, 341−349.
(36) Hujsak, K. A.; Roth, E. W.; Kellogg, W.; Li, Y.; Dravid, V. P. High speed/low dose analytical electron microscopy with dynamic sampling. *Micron* **2018**, *108*, 31−40.
(37) Zhou, L.; Song, J.; Kim, J. S.; Pei, X.; Huang, C.; Boyce, M.; Mendonça, L.; Clare, D.; Siebert, A.; Allen, C. S.; Liberti, E.; Stuart, D.; Pan, X.; Nellist, P. D.; Zhang, P.; Kirkland, A. I.; Wang, P. Low-dose phase retrieval of biological specimens using cryo-electron ptychography. *Nat. Commun.* **2020**, *11*, 2773.

https://doi.org/10.1021/acs.biomac.2c00323
Biomacromolecules XXXX, XXX, XXX−XXX